JOURNAL OF QUATERNARY SCIENCE (2025) 1–13 ISSN 0267-8179. DOI: 10.1002/jqs.3731

JQS Journal of Quaternary Science QRA Quaternary Research Association

Luminescence dating of palaeoshoreline deposits from Khyargas Nuur, Western Mongolia: A comparative study of multigrain and single-grain K-feldspar dating

NEDA RAHIMZADEH,[1]* DENNIS WOLF,[2] SUMIKO TSUKAMOTO,[1,3] MANFRED FRECHEN[1] and FRANK LEHMKUHL[2]
[1]Leibniz Institute for Applied Geophysics, Hannover, Germany
[2]Department of Geography, RWTH Aachen University, Aachen, Germany
[3]Department of Geosciences, University of Tübingen, Tübingen, Germany

Received 29 January 2025; Revised 15 May 2025; Accepted 2 June 2025

ABSTRACT: The evolution of lakes in western Mongolia and their responses to climate changes and glacial meltwater input remain poorly understood. This study evaluates the reliability of multigrain and single-grain K-feldspar post-infrared infrared stimulated luminescence (IRSL) (pIRIR) dating applied to palaeoshoreline sediments at Khyargas Nuur, western Mongolia. It specifically focuses on assessing the extent of pIRIR signal bleaching and proposes an improved methodology for dating shoreline sediments where quartz is unsuitable for luminescence dating. Multigrain pIRIR signals measured at 150°C (pIRIR$_{150}$) and 225°C (pIRIR$_{225}$) were used to date Holocene and older samples, respectively. Single-grain pIRIR dating was conducted for the first time in the region to assess bleaching conditions and refine age estimates. Our comprehensive methodological approach was essential for constructing a robust lake level chronology. Single-grain measurements, combined with the application of the minimum age model (MAM), allowed us to identify and correct for incomplete bleaching in several samples. Notably, many of the multigrain aliquots showed no clear signs of poor bleaching in their equivalent dose (D_e) distributions, which would have resulted in significant age overestimation if single-grain data had not been available. Without this approach, the chronology of lake level fluctuations could have been significantly misinterpreted. By addressing this issue, we confidently date the highest lake level at ~129 m above modern lake (a.m.l) to marine isotope stage (MIS) 5 (~89 ka) and a subsequent highstand (~118 m a.m.l) to the Late Glacial (~14 ka). Following this highstand, lake levels declined rapidly (~25 m/ka), reaching ~20 m a.m.l through the Late Glacial to early Holocene transition. During the late Holocene, the palaeolake experienced a gradual regression to ~7 m a.m.l before reaching its current elevation of 1029 m above sea level (a.s.l).

KEYWORDS: optical dating; multigrain; single-grain; lake level changes; Central Asia

Introduction

Endorheic drainage systems are widespread in the arid and semiarid regions of Mongolia, and terminal lakes can be suitable indicators of the climatic conditions and water balance within their catchments (Klinge and Sauer, 2019). Therefore, lake level changes can provide valuable information about palaeoatmospheric circulation, palaeoclimate and landscape evolution. Mongolia is located at the confluence of the mid-latitude Westerlies and the East Asian Monsoon. Thus, it is influenced by both systems, resulting in a complex and variable climate pattern on different timescales (Chen et al., 2019). Numerous studies have focused on reconstructing late Quaternary hydroclimatic history and understanding lake system responses in Mongolia (e.g., Grunert et al., 2000; Lehmkuhl et al., 2018; Klinge and Sauer, 2019; Zhang et al., 2022b). However, due to the intricate interactions between these atmospheric circulation systems, the hydroclimatic history of Mongolia during the late Quaternary remains only partially understood.

Western Mongolia contains the largest lakes in the region, covering approximately 9500 km^2, with the most prominent types being tectonic and glacial lakes (Orkhonselenge et al., 2022). The Depression of Great Lakes encompasses several lake basins, including Uvs Nuur, Khyargas Nuur and Khar-Us Nuur, the three largest lakes in this region (Fig. 1(a)). While numerous studies have investigated lakes in this region (e.g., Uvs Nuur: Grunert et al., 2000; Tsetseg Nuur: Klinge and Lehmkuhl, 2013; Bayan Nuur: Naumann, 1999; Grunert et al., 2000; Khoton Nuur: Klinge and Lehmkuhl, 2013; Lehmkuhl et al., 2016; Tsagaan Nuur: Klinge and Lehmkuhl, 2013; Khar Us Nuur: Lehmkuhl et al., 2016), the evolution of Khyargas Nuur has been largely overlooked, despite its potential to provide valuable insights into late Quaternary hydroclimatic history.

Radiocarbon (^{14}C) and optically stimulated luminescence (OSL) dating approaches are the two most commonly applied methods for dating palaeoshorelines and reconstructing lake level evolution. However, the application of radiocarbon dating to lacustrine sediments is often challenging due to limited availability of suitable organic materials and the reservoir effect (Long et al., 2015). Therefore, OSL dating has become the preferred method for dating shorelines and lacustrine sediments (Jacobs, 2008), though it may encounter

*Correspondence: Neda Rahimzadeh, as above.
Email: Neda.Rahimzadeh@liag-institut.de

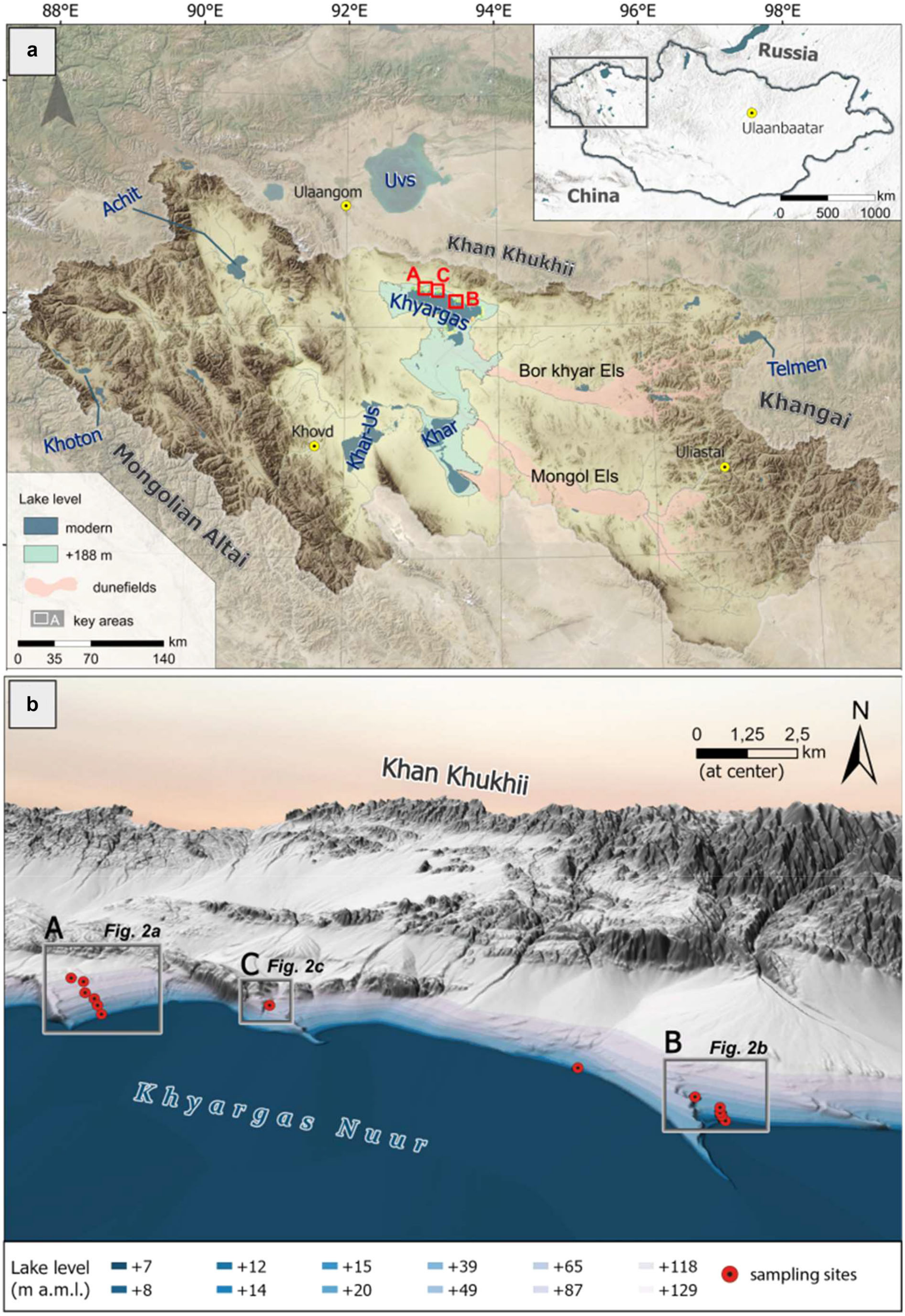

Figure 1. (a) Locations of Khyargas Nuur and other lakes in western Mongolia (based on the Copernicus GLO-30 DEM; European Space Agency, 2024) and (b) study region on the northern side of Khyargas Nuur, modified after Wolf et al. (2025). [Color figure can be viewed at wileyonlinelibrary.com]

challenges, particularly with incomplete bleaching in waterlain sediments. Although the quartz OSL signal is preferred for its rapid bleaching properties, OSL dating of quartz in Mongolia is often challenging due to the low intensity of the quartz OSL signal and significant feldspar contamination within quartz grains (Hülle et al., 2010; Li et al., 2023). An alternative is to use the infrared stimulated luminescence (IRSL) signals from K-feldspar, which generally offers a brighter signal and higher sensitivity to radiation dose. However, the K-feldspar IRSL signal bleaches much more slowly than the quartz OSL signal (Murray et al., 2012), which can lead to age overestimations. Single-grain optical dating offers a solution by enabling direct assessment of incomplete bleaching and supporting more accurate age estimates using an appropriate statistical age model, for example, minimum age model (MAM; Galbraith et al., 1999).

Recently, Wolf et al. (2025) presented the lake level evolution of Khyargas Nuur. In this study, we evaluated the bleaching characteristics of 19 samples from 12 palaeoshoreline sequences at Khyargas Nuur, which were used in Wolf et al. (2025). Luminescence properties of the shoreline sediments were first assessed using multigrain K-feldspar post-infrared IRSL (pIRIR) techniques. We also conducted the first single-grain K-feldspar pIRIR dating of lake shoreline deposits in western Mongolia. The single-grain results are compared with their multigrain counterparts to address incomplete bleaching of the pIRIR signal.

Material and methods

Study area and sampling

The Great Lakes Depression, western Mongolia, is located between the Mongolian Altai (<4300 m above sea level (a.s.l)) in the west and the Khangai Mountains (<4000 m a.s.l) in the east (Fig. 1(a)). Located in the rain shadow of the Altai Mountains, the Depression of Great Lakes is one of the most continental regions on Earth, characterised by extreme temperature variations and low precipitation. Consequently, the Quaternary landscape features, including alluvial fans, palaeolake deposits, beach ridges and dune fields, cover the surrounding basin. Khyargas Nuur, located in the centre of this vast tectonic depression, is the second largest tectonic lake (1029 m a.s.l, 1348.2 km^2) in the Great Lakes Depression. Two smaller lakes, Khar-Us Nuur (1157 m a.s.l, 946.49 km^2) and Khar Nuur (1130 m a.s.l, 561.96 km^2), are located to the south of the Khyargas Nuur. Evidence from elevated beach bars indicates that these three lakes were once part of a larger palaeolake system (Lehmkuhl et al., 2018). Eastward of these lakes, near the foothills of the Khangai Mountains, two dune fields, called Bor Khyar Els and Mongol Els, are located (Fig. 1(a)). These dune fields are the result of a long-term Pleistocene sediment cycle, involving fluvial sand transport to the basins and wind transport that dispersed silt-sized particles while depositing sand masses in the dune fields towards the east. The west–east orientation of the dune fields suggests that their formation is a result of deflation from the exposed lacustrine sediments by strong westerly winds during former arid periods (Lehmkuhl et al., 2024).

Palaeoshorelines in Khyargas Nuur are well preserved and can be clearly observed from satellite imagery (Fig. 2). A total of 14 beach ridges, assigned to 12 distinct palaeolake levels between 7 m above modern lake (a.m.l) and 129 m a.m.l, were identified (Figs. 1(b) and 2). According to the spatial distribution of the palaeoshorelines, we investigated three areas along the northern shore of Khyargas Nuur (study areas A, B and C; Fig. 1(b)). Study area A comprises seven sites (P01–P07) and features an extensive sequence of relict beach ridges extending from the current lake level up to ~129 m a.m.l (P03) (Fig. 2(a)). Study area B, which includes six sites (P11–12 and P22–25), is characterised by palaeoshorelines with elevations ranging from ~7 m a.m.l (P22) to ~39 m a.m.l (P12) (Fig. 2(b)). Study area C, at an elevation of 87 m a.m.l, comprises a single, well-exposed section (P14) located within a recently formed channel that has incised into an alluvial fan (Fig. 2(c)). The lacustrine nature of individual layers in this section is evident from the presence of lake-derived sediments containing microfossils, confirming its palaeolake origin (Wolf et al., 2025). The section begins beneath a ~3 m thick upper layer of the fan body (e.g., angular gravels and poorly sorted alluvial deposits) and shows alternating layers of coarse (fine gravel to coarse sand) and fine (fine sand to silt) material (Fig. S1(c)). All investigated sites are mainly composed of well-sorted gravels and coarse sands with cross- or inclined bedding structures, exhibiting the typical sedimentary characteristics of beach deposits (Fig. S1). A total of 19 luminescence samples (Table 1) were collected from 12 distinct palaeolake level elevations using opaque luminescence sampling tubes, which were hammered into freshly cleaned sections. For the two palaeolake levels, overlapping samples were taken from different sites: between study areas A and B (P07 and P11) at 14 m a.m.l and between study areas A and C (P04 and P14) at 87 m a.m.l. Dose rate samples were taken from the same position as the luminescence samples and their immediate surroundings.

Sample preparation

OSL sample preparation was carried out under subdued red-light conditions in the luminescence laboratory at the Leibniz Institute for Applied Geophysics (LIAG) in Hannover, Germany. To minimise the risk of light exposure, ~2 cm from each end of the sampling tubes was removed. The remaining inner material was treated with hydrochloric acid (HCl, 10%), sodium oxalate ($Na_2C_2O_4$, 0.1 N) and hydrogen peroxide (H_2O_2, 30%) to remove carbonate, mineral aggregates and organic matter, respectively. After chemical treatments, the samples were dry-sieved using sieves of 100, 150, 200 and 250 µm aperture sizes. Given that OSL properties of quartz from Mongolia have been reported to be poor and often suffer from severe feldspar contamination that cannot be fully eliminated (e.g., Hülle et al., 2010; Li et al., 2023), our measurements focused on K-feldspar minerals. K-feldspar grains (150–200 µm) were separated from quartz and other minerals using a heavy liquid solution (sodium polytungstate; $\rho \leq 2.58$ g cm^{-3}). Grains were mounted onto stainless steel discs using silicone spray with diameters of either 1 mm or 2.5 mm for single-aliquot measurements and onto aluminium discs with a 10 × 10 grid of holes (each 300 µm in diameter and 300 µm deep) for single-grain measurements.

Luminescence equipment and measurement conditions

Multigrain measurements

Luminescence measurements were performed using an automated Risø TL/OSL-15 reader equipped with blue (470 ± 30 nm) and infrared (870 ± 40 nm) LEDs and calibrated ^{90}Sr/^{90}Y beta source with a dose rate of 0.089 Gy s^{-1}. All signals were detected through a combination of Schott BG-39/Corning 7-59 filters. A single aliquot regenerative (SAR; Murray and Wintle, 2000) protocol adapted for feldspars as post-infrared IRSL (pIRIR; Thomsen et al., 2008) protocol was used for the equivalent dose (D_e) measurement. The pIRIR signals from the first IR bleaching at 50°C and subsequent IR stimulation at 150°C (pIRIR$_{150}$; Reimann and

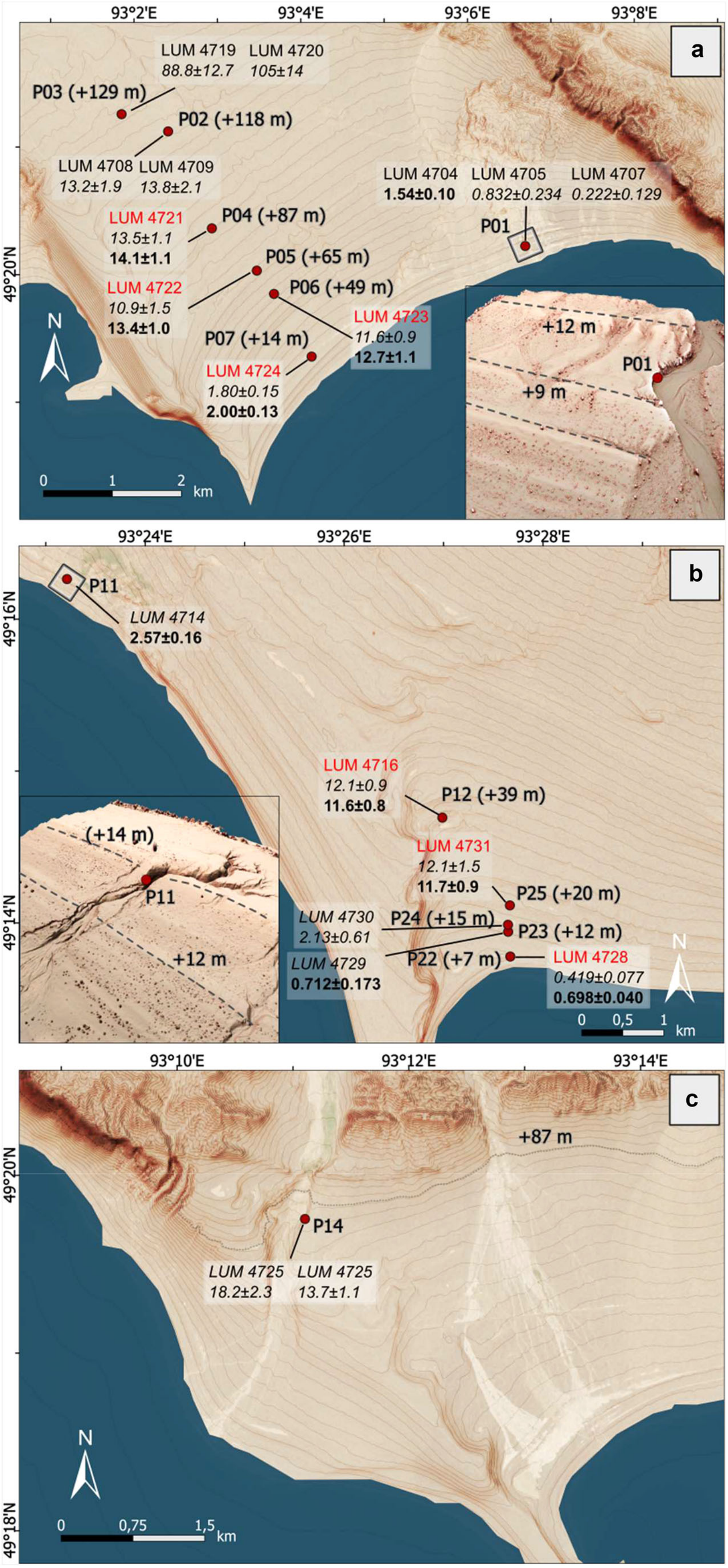

Figure 2. (a, b and c) remote sensing images of study areas A, B and C, respectively, showing the distribution of palaeoshoreline and sampling locations (modified after Wolf et al. (2025)). Ages shown in italic were measured using the single-grain approach, while ages in bold represent measurements using the multigrain approach. Sample numbers in red indicate well-bleached samples, with both single-grain (italic) and multigrain (bold) ages. [Color figure can be viewed at wileyonlinelibrary.com]

Tsukamoto, 2012) were measured for Holocene samples (Table 2). With regard to the older samples, the pIRIR signals at 225°C (pIRIR$_{225}$; Buylaert et al., 2009) were measured (Table 2). The signals were analysed using the initial signal derived from the first 5 s and 3 s of the pIRIR$_{150}$ and pIRIR$_{225}$ signals, respectively. A late background subtraction using the last 15 s for pIRIR$_{150}$ and 25 s for the pIRIR$_{225}$ was applied. For each sample, 15 to 24 aliquots with 2.5 mm diameter were measured and arithmetic mean D_e was

Table 1. Details of sample locations, measured radionuclide concentrations determined using gamma spectrometry, and the corresponding calculated environmental dose rates.

LUM No.	Section	Elevation of sample (m)	Elevation above lake level (m)	Depth below surface (m)	U (ppm)	Th (ppm)	K (%)	Dose rate (Gy ka^{-1})
4704	P01	1037	8	1.8	2.19 ± 0.11	6.79 ± 0.34	2.31 ± 0.12	4.08 ± 0.18
4705	P01	1037	8	1.2	2.83 ± 0.14	10.1 ± 0.51	2.38 ± 0.12	4.56 ± 0.19
4707	P01	1037	8	0.5	2.75 ± 0.14	10.2 ± 0.51	2.48 ± 0.12	4.66 ± 0.19
4708	P02	1146	118	0.7	1.73 ± 0.09	4.66 ± 0.23	1.60 ± 0.08	3.20 ± 0.15
4709	P02	1146	118	1.2	1.82 ± 0.09	4.61 ± 0.23	1.59 ± 0.08	3.19 ± 0.15
4714	P11	1045	14	2.5	2.51 ± 0.13	7.47 ± 0.37	2.08 ± 0.10	3.98 ± 0.17
4716	P12	1070	39	0.4	1.55 ± 0.08	3.91 ± 0.20	1.74 ± 0.09	3.26 ± 0.15
4719	P03	1158	129	0.5	1.50 ± 0.08	3.33 ± 0.17	1.60 ± 0.08	3.07 ± 0.15
4720	P03	1158	129	1.2	2.26 ± 0.11	5.13 ± 0.26	1.48 ± 0.07	3.23 ± 0.15
4721	P04	1108	87	0.6	2.20 ± 0.11	5.96 ± 0.30	1.95 ± 0.10	3.73 ± 0.16
4722	P05	1090	65	0.7	1.73 ± 0.09	4.26 ± 0.22	2.01 ± 0.10	3.55 ± 0.16
4723	P06	1071	49	0.6	1.48 ± 0.07	3.79 ± 0.19	2.42 ± 0.12	3.84 ± 0.18
4724	P07	1041	14	0.5	1.49 ± 0.08	4.25 ± 0.21	2.36 ± 0.12	3.83 ± 0.17
4725	P14	1078	87	3.3	2.65 ± 0.13	7.06 ± 0.35	1.92 ± 0.10	3.82 ± 0.17
4726	P14	1078	87	5.8	2.01 ± 0.10	5.99 ± 0.30	1.77 ± 0.09	3.40 ± 0.15
4728	P22	1036	7	0.2	1.64 ± 0.08	3.30 ± 0.17	1.66 ± 0.08	3.20 ± 0.15
4729	P23	1041	12	0.4	1.48 ± 0.07	2.69 ± 0.14	1.38 ± 0.07	2.82 ± 0.14
4730	P24	1044	15	0.4	1.76 ± 0.09	3.33 ± 0.17	1.73 ± 0.09	3.26 ± 0.15
4731	P25	1049	20	0.4	1.65 ± 0.08	3.65 ± 0.18	1.75 ± 0.09	3.28 ± 0.15

Table 2. Measurement protocols used in this study.

Step	K-feldspar multigrain $pIRIR_{150}$ protocol (Reimann and Tsukamoto, 2012)	Observed	K-feldspar single-grain $pIRIR_{150}$ protocol	Observed
1	Given dose		Given dose	
2	Preheat at 180°C for 60 s		Preheat at 180°C for 60 s	
3	IRSL, 100 s at 50°C		IRSL, 100 s at 50°C	
4	IRSL, 200 s at 150°C	L_x	IR laser, 2 s at 150°C	L_x
5	Given test dose		Given test dose	
6	Preheat at 180°C for 60 s		Preheat at 180°C for 60 s	
7	IRSL, 100 s at 50°C		IRSL, 100 s at 50°C	
8	IRSL, 100 s at 150°C	T_x	IR laser, 2 s at 150°C	T_x
9	Return to 1		Return to 1	

Step	K-feldspar multigrain $pIRIR_{225}$ protocol (Buylaert et al., 2009)	Observed	K-feldspar single-grain $pIRIR_{225}$ protocol	Observed
1	Given dose		Given dose	
2	Preheat at 250°C for 60 s		Preheat at 250°C for 60 s	
3	IRSL, 100 s at 50°C		IRSL, 100 s at 50°C	
4	IRSL, 200 s at 225°C	L_x	IR laser, 2 s at 225°C	L_x
5	Given test dose		Given test dose	
6	Preheat at 250°C for 60 s		Preheat at 250°C for 60 s	
7	IRSL, 100 s at 50°C		IRSL, 100 s at 50°C	
8	IRSL, 200 s at 225°C	T_x	IR laser, 2 s at 225°C	T_x
9	IRSL, 100 s bleaching at 290°C		IRSL, 100 s bleaching at 290°C	
10	Return to 1		Return to 1	

calculated. Additionally, 48 small aliquots with 1 mm diameter were measured for samples LUM 4704, 4714 and 4729 (Table 3). Dose response curves (DRC) were constructed by fitting the sensitivity-corrected regenerative signals (L_x/T_x) with a single exponential function (Fig. 3(a),(b)). Aliquots were accepted if the recycling ratio was within 10% of unity, the recuperation signal was <5% of the natural signal (or <5% of the largest regenerative dose for some very young samples) and the signal was $>3\sigma$ above the background. The reliability of the protocols was tested by conducting dose recovery experiments on all samples. Six aliquots were bleached in the solar simulator (Hönle SOL2) for 4 h. Three bleached aliquots were used to determine the residual dose. The other three bleached aliquots were given a dose close to the natural D_e and subsequently were measured by the protocols. The dose recovery ratio was calculated by dividing the measured dose (residual dose subtracted) by the given dose.

Laboratory fading rate ($g_{2\text{days}}$ value) was measured following Auclair et al. (2003) with three to four aliquots for each sample. All samples were corrected for anomalous fading using sample-specific fading rates. The fading correction method of Huntley and Lamothe (2001) was performed for samples with fading-uncorrected ages of <50 ka (signal in the linear range of the DRC). For older samples (i.e., LUM 4719 and 4720), the Kars et al. (2008) fading correction method was used.

Single-grain measurements

Lacustrine and shoreline sediments are often susceptible to incomplete bleaching of the luminescence signal prior to deposition, particularly for the feldspar pIRIR signal (Rhodes, 2011). One method to evaluate the potential for incomplete bleaching is to make use of the differential

Table 3. Summary of post-infrared infrared stimulated luminescence (pIRIR) dating results from multigrain measurements.

LUM No.	Section	Protocol	Aliquot size (mm)	n.al.acc/ meas.	D_e (Gy)	OD (%)	$g_{2\text{days}}$ value (%/decade)	Age (ka) uncorr.[a]	Age (ka) corr.[a,b]
4704	P01	pIRIR$_{150}$	2.5	24/24	5.72 ± 0.18	13 ± 2	1.28 ± 0.38	1.40 ± 0.08	1.54 ± 0.10
			1	38/47	5.51 ± 0.25	22 ± 3			
4705	P01	pIRIR$_{150}$	2.5	24/24	91.3 ± 8.2	43 ± 6	1.84 ± 0.38	20.0 ± 2.0	23.6 ± 2.5
4707	P01	pIRIR$_{150}$	2.5	21/21	24.8 ± 3.6	64 ± 10	1.47 ± 0.40	5.32 ± 0.81	6.30 ± 1.02
4708	P02	pIRIR$_{225}$	2.5	24/24	127 ± 8	29 ± 4	2.05 ± 0.39	39.7 ± 3.1	48.0 ± 4.5
4709	P02	pIRIR$_{225}$	2.5	24/24	148 ± 14	41 ± 6	2.12 ± 0.38	46.4 ± 4.8	56.6 ± 6.6
4714	P11	pIRIR$_{150}$	2.5	17/24	9.74 ± 1.11	35 ± 6	1.82 ± 0.39	***2.22 ± 0.12***	***2.57 ± 0.16***
			1	32/48	8.83 ± 0.32	17 ± 3			
4716	P12	pIRIR$_{150}$	2.5	24/24	33.6 ± 0.8	11 ± 2	1.40 ± 0.44	10.3 ± 0.5	11.6 ± 0.8
4719	P03	pIRIR$_{225}$	2.5	15/15	292 ± 9	14 ± 3	2.19 ± 0.38	95.0 ± 5.8	147 ± 9
4720	P03	pIRIR$_{225}$	2.5	15/15	342 ± 13	11 ± 2	2.12 ± 0.39	106 ± 7	167 ± 12
4721	P04	pIRIR$_{225}$	2.5	24/24	47.2 ± 1.0	10 ± 2	1.22 ± 0.58	12.7 ± 0.6	14.1 ± 1.1
4722	P05	pIRIR$_{225}$	2.5	23/24	44.1 ± 0.9	8 ± 1	0.91 ± 0.55	12.4 ± 0.6	13.4 ± 1.0
4723	P06	pIRIR$_{225}$	2.5	23/24	41.0 ± 0.5	5 ± 1	1.43 ± 0.53	10.7 ± 0.5	12.7 ± 1.1
4724	P07	pIRIR$_{150}$	2.5	23/24	6.75 ± 0.19	12 ± 2	1.63 ± 0.39	1.76 ± 0.09	2.00 ± 0.13
4725	P14	pIRIR$_{225}$	2.5	23/24	126 ± 5	19 ± 3	1.69 ± 0.39	32.1 ± 1.9	37.4 ± 2.7
4726	P14	pIRIR$_{225}$	2.5	24/24	147 ± 8	25 ± 4	1.61 ± 0.38	42.6 ± 3.0	49.4 ± 4.0
4728	P22	pIRIR$_{150}$	2.5	21/24	2.09 ± 0.00	24 ± 4	1.00 ± 0.42	0.654 ± 0.030	0.698 ± 0.040
4729	P23	pIRIR$_{150}$	2.5	15/24	3.57 ± 0.25	24 ± 5	1.48 ± 0.42	***0.636 ± 0.151***	***0.712 ± 0.173***[c]
			1	34/56	1.79 ± 0.41[b]	73 ± 9			
4730	P24	pIRIR$_{150}$	2.5	18/20	21.0 ± 2.1	42 ± 7	1.05 ± 0.42	7.24 ± 0.75	7.91 ± 0.91
4731	P25	pIRIR$_{150}$	2.5	23/24	33.6 ± 0.9	10 ± 2	1.54 ± 0.65	10.3 ± 0.5	11.7 ± 0.9

n.al.acc/meas. = number of accepted/measured aliquots; OD = overdispersion; (un)corr. = (un)corrected.

[a] Ages in bold italics were calculated using the 1 mm aliquots, while the others were calculated using the 2.5 mm aliquots.

[b] The age results have since been incorporated into a related applied study by Wolf et al. (2025), except for the ages from site P01.

[c] The D_e value and the age were calculated using minimum age model (MAM).

bleaching rates of quartz and feldspar luminescence signals, as these two dosimeters show different bleaching behaviour (Murray et al., 2012; Colarossi et al., 2015). However, a comparison between quartz OSL and K-feldspar pIRIR ages is not possible here due to the poor characteristics of the quartz OSL signal. An alternative method for identifying incomplete bleaching in the pIRIR signal is to compare the IR$_{50}$ and pIRIR ages. The pIRIR measurement yields two luminescence signals with different properties: the lower temperature IR$_{50}$ signal, which bleaches more rapidly, and the elevated temperature pIRIR signal, which is more stable and less affected by anomalous fading. This difference can be used to assess potential incomplete bleaching of the pIRIR signal. This will be further discussed in Section 3.1. A third method to assess the likelihood of incomplete bleaching is to investigate the characteristics of the D_e distributions, such as overdispersion (OD; Galbraith et al., 1999). Although this statistical parameter is based on single-grain measurements, it may be used as an approximation for multigrain aliquots. The large OD value observed in some of the investigated samples suggests they may have experienced poor bleaching (Table 3). Therefore, single-grain measurements of K-feldspar were performed to further investigate the potential for incomplete bleaching of the pIRIR signal.

The single-grain measurement follows the same procedure as the multigrain measurement, except that the 200 s IR diode stimulation was replaced with a 2 s IR laser (830 nm) stimulation (Table 2). Laboratory irradiation was carried out using a calibrated ^{90}Sr/^{90}Y beta source with a dose rate of 0.111 Gy s^{-1}. The pIRIR signal was detected with the combination of Schott BG-39/Corning 7-59 filters. For each sample, three to six single-grain discs (300–600 grains) were measured, and the signal from the initial 0.1 s stimulation minus a background from the last 0.2 s of the decay curves was used for D_e determination. All DRCs were fitted using a single exponential function (Fig 4(a),(b)). Grains with poor IRSL properties were excluded based on the following criteria: (1) the initial T_n signal was less than 3σ of the corresponding background signal, or the relative error of T_n exceeded 20%; (2) the recycling ratio was not within the range of 0.85–1.15; (3) the recuperation ratio was greater than 5%; (4) the figure of merit (FOM) exceeded 10%; (5) the reduced chi-square (RCS) value for the DRC was >5; (6) the D_e uncertainty could not be estimated; and (7) the L_n/T_n value reached or exceeded the saturation level of the DRC, and therefore a finite D_e value and error cannot be obtained. The numbers of grains measured, rejected and accepted for each sample, along with the reasons for rejection, are summarised in Table S1. The rejection procedure described above and the single-grain D_e estimation were achieved using the 'numOSL' R package (Peng and Li, 2017).

Residual dose and dose recovery tests were conducted on samples LUM 4723 and 4724 to evaluate the suitability of the pIRIR$_{225}$ and pIRIR$_{150}$ protocols, respectively. Three single-grain discs (300 grains) were prepared for each sample and bleached for 4 h in the solar simulator. The fading rates obtained from the multigrain measurements were used to correct the single-grain pIRIR ages.

Dose rate determination

Material taken from the nearby surroundings of each luminescence sample was dried, homogenised, filled into 50 g plastic container, sealed and stored for at least 4 weeks to ensure equilibrium of ^{222}Rn. The radionuclide concentration of U, Th and K was determined by high-resolution gamma spectrometry. The environmental dose rate for each sample was calculated using the conversion factor of Liritzis et al. (2013), beta attenuation factor of Guérin et al. (2012) and assuming a water content of 6 ± 4%. The large relative uncertainty was used to account for the possible alterations in water content over geological time. A small cosmic dose rate of <0.3 Gy ka^{-1} was determined based on Prescott and Hutton (1994). An additional internal beta dose rate was calculated based on a

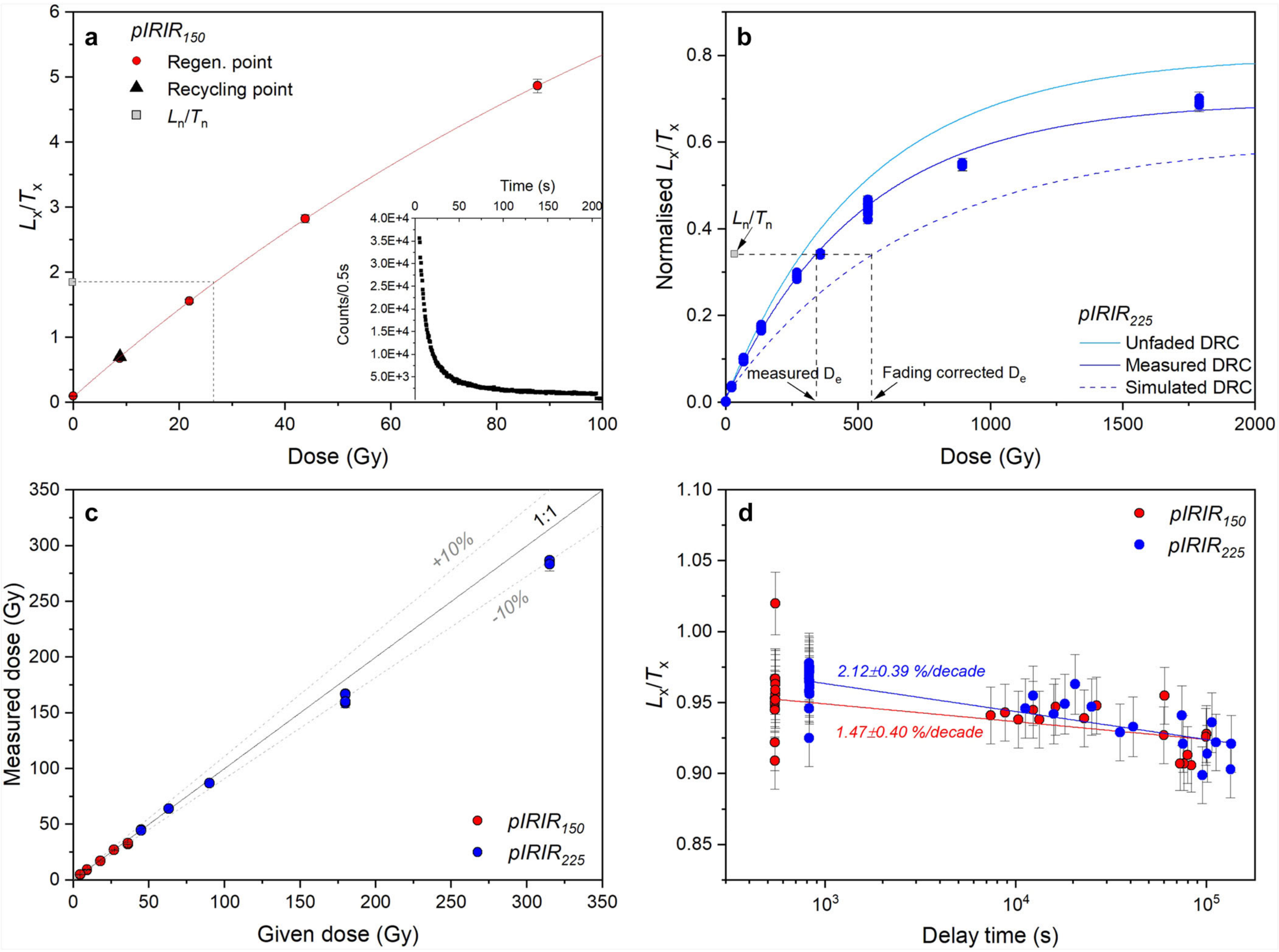

Figure 3. (a) Normalised sensitivity-corrected pIRIR$_{150}$ dose response and natural decay curve (inset) for an aliquot of sample LUM 4707, (b) measured, unfaded and fading-corrected dose response curve of pIRIR$_{225}$ for sample LUM 4720, (c) results of the dose recovery tests for all samples and (d) fitting of luminescence sensitivity and delay time of pIRIR$_{150}$ and pIRIR$_{225}$ for samples LUM 4707 and 4720, respectively. [Color figure can be viewed at wileyonlinelibrary.com]

K concentration of 12.5 ± 0.5% (Huntley and Baril, 1997) and a rubidium content of 400 ± 100 ppm (Huntley and Hancock, 2001). Information on U, Th and K contents and total dose rates are summarised in Table 1.

Results and discussion

K-feldspar multigrain aliquot pIRIR dating

Representative pIRIR$_{150}$ and pIRIR$_{225}$ DRCs that met the rejection criteria are shown in Fig. 3(a) and (b), respectively. The reliability of the multigrain pIRIR protocols was tested using standard performance tests, that is, residual dose, dose recovery and signal stability tests, for all samples. The residual doses of pIRIR signals persisting after 4 h of solar simulator bleaching range from 0.04 ± 0.08 Gy (LUM 4714) to 4.43 ± 0.31 Gy (LUM 4720). The dose recovery ratios for all samples were within 10% of unity (Fig. 3(c)). The stability of pIRIR signals was checked by determining $g_{2\text{days}}$ values. The average $g_{2\text{days}}$ values were 1.44 ± 0.07%/decade and 1.68 ± 0.14%/decade for pIRIR$_{150}$ and pIRIR$_{225}$, respectively (Table 3). Figure 3(d) shows the anomalous fading test results for the pIRIR$_{150}$ and pIRIR$_{225}$ signals of samples LUM 4707 and 4720, respectively. An example of the fading correction of the pIRIR$_{225}$ age, following Kars et al. (2008), is presented in Fig 3(b)).

As previously mentioned, assessing the bleaching condition of pIRIR signals is crucial for lacustrine and shoreline deposits. Initial concerns about poor bleaching of samples were raised by the large OD values in multigrain measurements (i.e., 2.5 mm aliquot), which ranged from 5% to 64% (Table 3). To further evaluate the degree of bleaching, we compared the fading-corrected IR$_{50}$ and pIRIR ages. Since the IR$_{50}$ signal bleaches much faster than the pIRIR signals (i.e., pIRIR$_{150}$ and pIRIR$_{225}$; Reimann and Tsukamoto, 2012; Colarossi et al., 2015), the pIRIR signals can be considered well-bleached if their ages are consistent with the corresponding IR$_{50}$ ages. The comparison between fading-corrected IR$_{50}$ and pIRIR ages shows general consistency for most samples, with a tendency for IR$_{50}$ age underestimation (Fig. S2(a)). However, it should be noted that the $g_{2\text{days}}$ values of the IR$_{50}$ signal were >~3.5%/decade (Table S2), suggesting that fading overcorrection of IR$_{50}$ ages may obscure the effects of partial bleaching in the pIRIR signals. To explore this, a numerical experiment was conducted using 7 well-bleached samples (LUM 4716, 4721–4724, 4728 and 4731; see Section 3.2). In this experiment, fading-corrected pIRIR ages were used as reference ages. The IR$_{50}$ ages were then recalculated using a range of assumed $g_{2\text{days}}$ values ranging from 1% to 6%/decade, plotted against the corresponding pIRIR reference ages and fitted with a linear function. The numerical simulation showed that fading-corrected IR$_{50}$ ages significantly deviated from the

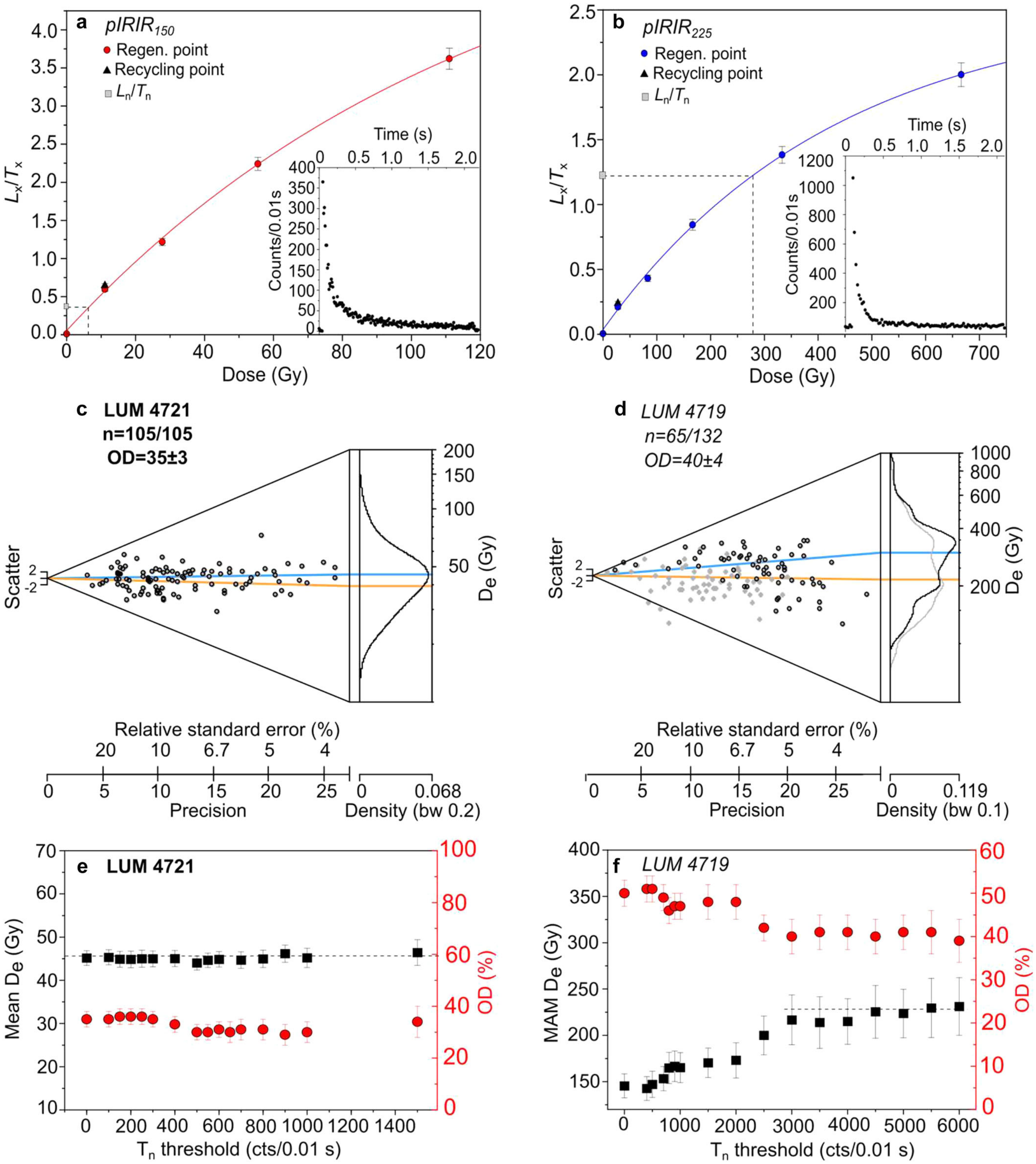

Figure 4. (a,b) Normalised sensitivity-corrected dose response and natural decay curve (inset) of K-feldspar single-grain pIRIR$_{150}$ (a) and pIRIR$_{225}$ (b) protocols for samples LUM 4707 and 4720, respectively. (c,d) Abanico plots illustrating the D_e distribution of K-feldspar single-grains for a well-bleached sample (c) and a poorly bleached sample (d). Bold sample number corresponds to well-bleached sample, while those in italics represent poorly bleached sample. n = number of grains used for D_e calculation (black circles)/number of grains passing standard selection criteria (grey circles). OD values indicate the overdispersion of the grains used for the D_e calculation (black circles). The blue lines represent the arithmetic mean D_e, and the orange lines indicate the minimum age model (MAM) D_e. (e,f) D_e (in black) and OD (in red) values plotted as a function of T_n threshold for samples LUM 4721 (e) and 4719 (f). The dashed lines represent the D_e plateau. [Color figure can be viewed at wileyonlinelibrary.com]

reference ages when $g_{2\text{days}}$ values are larger than 4%/decade (Fig. S2(b)), indicating overcorrection of IR$_{50}$ ages.

K-feldspar single-grain pIRIR dating

Figure 4(a) and (b) shows the dose response and decay curves for the pIRIR$_{150}$ and pIRIR$_{225}$ signals of K-feldspar single-grain, respectively. The signals decayed to background within 0.5 s, and the DRCs were successfully fitted with a single exponential function. The residual doses of the pIRIR$_{150}$ and pIRIR$_{225}$ signals for samples LUM 4724 and 4723 were −0.16 ± 0.05 Gy and 5.21 ± 0.39 Gy, respectively (Figs. S3(b) and S3(a)). After residual subtraction, the dose recovery ratios for samples LUM 4723 and 4724 were 1.08 ± 0.03 and

1.07 ± 0.06, respectively (Fig. S3(c),(d)), confirming the reliability of the pIRIR protocols.

Between 300 and 600 grains were measured for each sample. For samples LUM 4704, 4714 and 4729, only 1–2% of the total measured grains met all screening criteria (Table S1), making it impractical to obtain enough data for further analysis. As a result, 48 aliquots with 1 mm diameter were measured for these samples (Table 3). For the remaining samples, 6–36% of the total number measured were accepted and used to determine the single-grain D_{e}. The majority of grains were rejected because of weak signals (i.e., the initial intensity of T_{n} was less than 3σ above the background intensity and/or its relative standard error was more than 20%; Table S1).

The OD (Galbraith et al., 1999) and the distribution of single-grain D_{e} values (Bailey and Arnold, 2006) are commonly used as indicators of the extent of luminescence signal bleaching. Seven samples (LUM 4716, 4721–4724, 4728 and 4731) showed homogenous D_{e} distributions, characterised by low OD values (~17–35%; Table 4), with D_{e} values distributed mostly around the central value (Fig. S4(e),(h)–(k),(n),(p)), suggesting that these samples are well bleached (Bailey and Arnold, 2006). In contrast, the remaining nine samples (LUM 4705, 4707–4709, 4719–4720, 4725–4726 and 4730) exhibited more heterogeneous single-grain D_{e} distributions characterised by large OD values of up to ~96% (Table 4), with larger proportions of single-grain D_{e} values lying outside the 2 sigma range around the central value, along with more distinct leading edges of low D_{e} values or elongated tails of higher D_{e} values (Fig. S4(a)–(d),(f)–(g),(l)–(m),(o)), consistent with the characteristics of poorly bleached sediments (Bailey and Arnold, 2006). Representative single-grain D_{e} distributions for well-bleached and poorly bleached samples are shown in Fig. 4(c) and 4(d), respectively.

Previous studies have shown a relationship between D_{e} values and signal sensitivities (T_{n} intensity), where D_{e} values steadily increase with T_{n} intensity until they reach a plateau (Reimann et al., 2012; Guo et al., 2020; Zhang et al., 2022a). To explore this further, we examined the dependence of D_{e} on grain brightness by conducting 'T_{n} threshold plateau' test as described by Guo et al. (2020). In this test, the D_{e} and OD values of accepted grains were plotted against the minimum T_{n} responses (i.e., the T_{n} threshold) (Fig. S5). For well-bleached samples, the mean D_{e} was used, while for poorly bleached samples, the MAM D_{e} was applied. The result showed that with increasing the T_{n} threshold, that is, excluding the dim grains, the OD of most samples decreased. However, two different patterns were observed for D_{e} variations: (1) D_{e} values increased with T_{n} threshold and then reached a plateau (Fig. 4(f)), and (2) D_{e} values showed no obvious trend with changes in T_{n} threshold (Fig. 4(e)). For the first pattern, dim grains with underestimated D_{e} values were excluded, and grains with T_{n} above the lowest T_{n} threshold in the plateau region were selected for analysis. For the second pattern, as D_{e} values did not vary with grain brightness, all accepted grains were included in the D_{e} calculation.

For the poorly bleached samples, MAM was applied to calculate the final D_{e}. To implement the MAM, it is necessary to first determine the OD of the D_{e} distribution for well-bleached grains (i.e., σ_{b}; Galbraith et al., 1999). The OD of the D_{e} distribution of well-bleached samples, after excluding dim grains, can be used as the σ_{b} for MAM analysis (Reimann et al., 2012). The OD of the D_{e} distribution of the selected brightest grains of well-bleached samples ranged from ~17 to 35% (Table 4), and thus a σ_{b} value of 0.3 was selected for the MAM analysis. For well-bleached samples, the arithmetic mean D_{e} was used for the final D_{e} calculation. The resulting D_{e} values and corresponding ages are listed in Table 4.

Chronology of palaeoshorelines

The dating results from multigrain and single-grain measurements are presented in Tables 3 and 4, respectively. At study

Table 4. Summary of post-infrared infrared stimulated luminescence (pIRIR) dating results from single-grain measurements.

LUM No.	Section	Grain No.[a]	T_{n} threshold (cts/0.01 s)	Mean D_{e} (Gy)	MAM D_{e} (Gy)	OD (%)[b]	OD (%)[c]	Age (ka) uncorr.[d]	Age (ka) corr.[d,e]
4704	P01	0/9/400	—	—	—	—	—	—	—
4705	P01	52/52/400	All	31.0 ± 7.4	3.29 ± 0.91	95 ± 6	95 ± 6	0.721 ± 0.203	0.832 ± 0.234
4707	P01	69/69/400	All	1.91 ± 0.65	0.940 ± 0.589	58 ± 7	58 ± 7	0.202 ± 0.127	0.222 ± 0.129
4708	P02	36/69/300	700	133 ± 22	34.9 ± 4.6	87 ± 8	85 ± 10	10.9 ± 1.5	13.2 ± 1.9
4709	P02	69/69/400	All	170 ± 21	36.2 ± 5.0	96 ± 8	96 ± 8	11.3 ± 1.7	13.8 ± 2.1
4714	P11	0/9/400	—	—	—	—	—	—	—
4716	P12	28/67/600	400	34.8 ± 1.6	33.3 ± 2.3	31 ± 3	23 ± 3	***10.7 ± 0.7***	***12.1 ± 0.9***
4719	P03	65/132/400	3000	300 ± 17	217 ± 27	50 ± 3	40 ± 4	70.7 ± 9.4	88.8 ± 12.7[f]
4720	P03	35/70/400	1500	334 ± 21	271 ± 32	47 ± 4	37 ± 5	83.9 ± 10.8	105 ± 14[f]
4721	P04	105/105/400	All	45.2 ± 1.7	39.4 ± 3.0	35 ± 3	35 ± 3	***12.1 ± 0.7***	***13.5 ± 1.1***
4722	P05	86/86/400	All	35.5 ± 1.3	31.6 ± 2.2	32 ± 3	32 ± 3	***10.0 ± 1.3***	***10.9 ± 1.5***
4723	P06	55/95/400	400	39.4 ± 1.4	36.8 ± 2.3	29 ± 2	28 ± 3	***10.2 ± 0.6***	***11.6 ± 0.9***
4724	P07	35/35/400	All	6.06 ± 0.38	5.69 ± 0.56	29 ± 2	29 ± 2	***1.58 ± 0.12***	***1.80 ± 0.15***
4725	P14	42/122/400	1750	144 ± 22	59.3 ± 6.7	70 ± 5	75 ± 8	15.5 ± 1.9	18.2 ± 2.3
4726	P14	143/143/400	All	133 ± 13	40.2 ± 2.3	94 ± 6	94 ± 6	11.8 ± 0.9	13.7 ± 1.1
4728	P22	18/18/400	All	1.24 ± 0.22	1.50 ± 0.24	17 ± 4	17 ± 4	***0.389 ± 0.072***	***0.419 ± 0.077***
4729	P23	0/2/400	—	—	—	—	—	—	—
4730	P24	25/25/500	All	32.9 ± 3.8	6.40 ± 1.78	83 ± 12	83 ± 12	1.96 ± 0.55	2.13 ± 0.61
4731	P25	20/34/600	100	34.4 ± 3.1	30.7 ± 3.1	37 ± 5	26 ± 2	***10.5 ± 1.1***	***12.1 ± 1.5***

[a] The three grain numbers represent the total number of grains used for D_{e} calculation (left), the number of grains that passed the standard selection criteria (middle) and the total number of grains measured (right).

[b] OD values of the grains passing the selection criteria.

[c] OD values of the grains used for D_{e} calculation.

[d] Ages in bold italics were calculated using the arithmetic mean D_{e}, while the others were calculated using the minimum age model (MAM) D_{e}.

[e] The age results have since been incorporated into a related applied study by Wolf et al. (2025), except for the ages from site P01.

[f] The Huntley and Lamothe (2001) fading correction method was used.

area A (Fig. 2(a)), samples from site P01 (LUM 4704, 4705 and 4707) were excluded from the discussion because they were collected from a channel intersecting palaeoshorelines (Fig. 2(a) inset) and were interpreted as reworked lake sediments deposited by fluvial processes. The single-grain D_e distributions of samples from sites P02 and P03 are positively skewed (Fig. S4(c),(d),(f),(g)) and exhibit a wide spread in D_e values (OD > ~50%), indicating that the sediments were poorly bleached. Application of MAM to the single-grain D_e distribution of samples LUM 4719 and 4720 from site P03, located at an elevation of 129 m a.m.l, yielded D_e estimates of 217 ± 27 Gy and 271 ± 32 Gy, corresponding to fading-corrected ages of 88.8 ± 12.7 ka and 105 ± 14 ka, respectively, using the Huntley and Lamothe (2001) method. Here, one would expect that the application of Huntley and Lamothe (2001) is not appropriate for these two samples, as the natural signal is in the nonlinear part of DRC. The method of Kars et al. (2008) was also applied on these samples by interpolating the MAM D_e values from single-grain measurements onto the measured DRC obtained from multigrain measurements to estimate 'pseudo' MAM L_n/T_n ratio, based on the assumption that the individual K-feldspar grains share a common growth curve (e.g., Li et al., 2015, 2018). Finally, fading-corrected MAM D_es were derived by projecting the 'pseudo' MAM L_n/T_n ratios onto the simulated DRCs. The fading-corrected MAM ages following Kars et al. (2008) were 96.8 ± 15.7 ka and 121 ± 17 ka for LUM 4719 and 4720, respectively. These are consistent within one sigma with fading-corrected ages obtained using Huntley and Lamothe (2001), suggesting that both approaches can reliably correct for fading in the studied samples. It should be noted that the age of sample LUM 4719 is only used in the following discussion of lake level changes. LUM 4719 was taken from a layer in the upper part of section at 50 cm, which exhibits a landward inclination indicative of a backshore depositional environment (P03 in Fig. S1(a); Wolf et al., 2025), and therefore can be confidently attributed to the shoreline at 129 m a.m.l. However, LUM 4720 was sampled from a deeper layer at 120 cm, and its deposition time may therefore slightly predate the lake level highstand at 129 m a.m.l. For samples from the 118 m a.m.l palaeoshoreline (LUM 4708 and 4709), the MAM D_e estimates ranged from 34.9 ± 4.6 Gy to 36.2 ± 5.0 Gy, yielding fading-corrected ages of 13.2 ± 1.9 ka and 13.8 ± 2.1 ka, respectively. Both samples were taken from the upper 120 cm of the section, marked by intercalated layers with landward inclination, indicating foreshore to backshore sedimentation (P02 in Fig. S1(a); Wolf et al., 2025), and were therefore used in our discussion of lake level changes. The remaining sites from study area A (P04 to P07) presented normally distributed single-grain D_e values (Figs. S4(h)–(k)) with relatively low OD values (28–35%), suggesting well-bleached sediments. For these samples, fading-corrected ages from multigrain measurements and the arithmetic mean of single-grain D_e values were consistent within uncertainties, ranging from 14.1 ± 1.1 ka (LUM 4721 at 87 m a.m.l; multigrain) to 1.80 ± 0.15 ka (LUM 4724 at 14 m a.m.l; single-grain) (Tables 3 and 4).

At study area B (Fig. 2(b)), only nine grains from sample LUM 4714 (P11 at 14 m a.m.l) and two grains from sample LUM 4729 (P23 at 12 m a.m.l) out of 400 grains passed all screening criteria (Table S1), resulting in insufficient data for further single-grain analysis. Therefore, between 48 and 56 small aliquots with a 1 mm diameter were measured for these samples. Each 1 mm aliquot contains 10–20 grains and can be regarded as an approximation of single-grain dating. For LUM 4714, an OD value of 17% was derived for the small aliquot measurements, suggesting a well-bleached sample. An arithmetic mean D_e value of 8.83 ± 0.32 Gy and respective fading-corrected age of 2.57 ± 0.16 ka were obtained for this sample. However, a high OD value of 73% was observed for LUM 4729, suggesting a partially bleached sample. For this sample, a MAM D_e value of 1.79 ± 0.41 Gy with the associated fading-corrected age of 0.712 ± 0.173 ka was yielded. Single-grain measurements for sample LUM 4730 from site P24 (15 m a.m.l) showed a heterogeneous D_e distribution (Fig. S4(o)) characterised by a large OD value of 83%. A MAM D_e value of 6.40 ± 1.78 Gy and a fading-corrected age of 2.13 ± 0.61 ka were obtained. For samples from sites P12, P22 and P25 (LUM 4716, 4728 and 4731, respectively), single-grain data showed relatively tight D_e distributions (Fig. S4(e),(n),(p)), indicating that these samples are well bleached. Similar to the well-bleached samples from study area A (P04 to P07), the fading-corrected multigrain ages for these samples were consistent with the mean single-grain ages, ranging from 12.1 ± 0.9 ka (LUM 4716 at 39 m a.m.l; single-grain) to 0.419 ± 0.077 ka (LUM 4728 at 7 m a.m.l; single-grain).

At study area C (Fig. 2(c)), the single-grain D_e distributions for samples LUM 4725 and 4726 (P14 at 87 m a.m.l) were positively skewed, with a wide spread (OD up to 94%) and a distinct high tail (Figs. S4(l)–(m)). Consequently, MAM was applied, yielding fading-corrected ages of 18.2 ± 2.3 ka and 13.7 ± 1.1 ka for samples LUM 4725 and 4726, respectively. It has to be noted that the MAM age of sample LUM 4725 appears unreliable due to stratigraphic inconsistencies with the underlying sample (LUM 4726) and its inconsistency with other sample taken from the same palaeoshoreline elevation (LUM 4721). As a result, the age of LUM 4725 was excluded from the subsequent discussion on lake level changes.

Lake level changes since the mid-Pleistocene are presented in Fig. 5. It is acknowledged that for the well-bleached samples, the mean ages obtained from both methods are consistent within one sigma (LUM 4722 and 4728 overlap at two sigma) and seem equally reliable; therefore, both data sets were used in the discussion. However, for the poorly bleached samples, further discussion refers only to the MAM ages derived from the single-grain measurements, as corresponding multigrain ages significantly overestimate the true depositional age (Fig. 5; open red circles). A detailed interpretation of lake level evolution at Khyargas Nuur is provided in Wolf et al. (2025). In summary, our results indicate that Khyargas Nuur

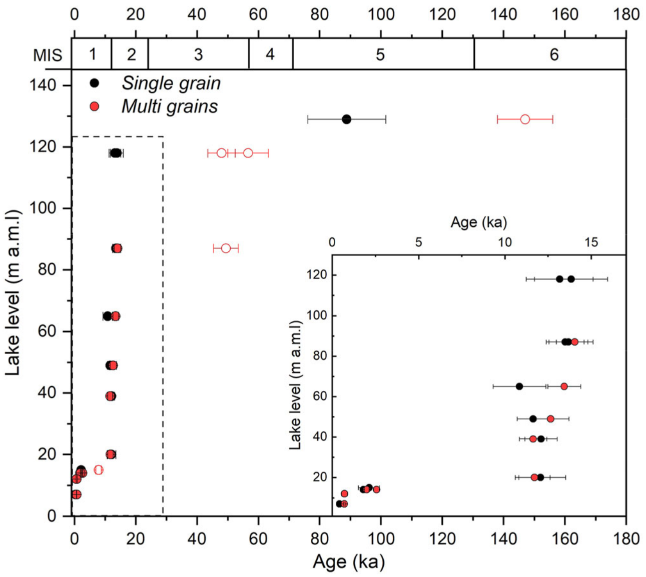

Figure 5. Lake level changes of Khyargas Nuur since MIS 5. Black and red circles represent single-grain and multigrain ages, respectively. The inset shows an enlarged view of the dashed box area. [Color figure can be viewed at wileyonlinelibrary.com]

experienced three distinct stages during the late Quaternary: (a) the highest lake level at 129 m a.m.l during Marine Isotope Stage (MIS 5) (88.8 ± 12.7 ka); (b) a high lake level at 118 m a.m.l during the Late Glacial, followed by rapid regression of about 100 m; and (c) a gradual regression during the late Holocene. This study underscores the critical importance of assessing the degree of bleaching in sediments from palaeolake shorelines. Incomplete bleaching may remain undetected in multigrain D_e distribution, that is, incomplete bleaching can be masked by averaging effects, potentially resulting in systematically overestimated ages if not evaluated through single-grain analysis. For example, if only multigrain data had been considered, the +129 m a.m.l shoreline would have been misattributed to MIS 6, and the +118 m a.m.l shoreline to MIS 3 (Fig. 5, open red circles), leading to significant misinterpretation of the lake level history. This highlights the essential role of single-grain dating in constraining accurate and reliable chronologies of lake level changes in settings prone to heterogeneous bleaching.

The geomorphological map of Mongolia, published by Deviatkin et al. (1987), showed the shorelines of large palaeolakes in western and southern Mongolia. In particular, three distinct palaeoshorelines were identified at Khyargas Nuur. The lowest, at 10–30 m a.m.l, indicates the presence of moderately expanded palaeolakes. The second shoreline, around 130 m a.m.l, corresponds to large palaeolakes. The highest shoreline, exceeding 300 m a.m.l, is evidence of giant palaeolake (Lehmkuhl et al., 2018). The Great Lakes Depression largely dried out during MIS 6 but reemerged during the last interglacial (MIS 5e) and persisted until the onset of the Last Glacial period (Orkhonselenge et al., 2022). In the Zavkhan Gol flood plain, eastern part of the Valley of the Great Lakes, the sand layers under lake deposits were dated to MIS 6, suggesting a dry phase during this period, and the formation of palaeolake after MIS 6. The high lake level of 250 m a.m.l in the Uvs Nuur basin, in northwestern Mongolia, was reported by Grunert et al. (2000). This elevated lake is hypothesised to have resulted from a potential hydrological connection between Bayan Nuur and Uvs Nuur. However, a few sedimentological evidence support this highstand, and no visible lacustrine deposits or shoreline features have been identified to confirm it. The exact timing of this highstand also remains uncertain. The radiocarbon dating of molluscs found in sands and silts of a deep-water environment (28 050 ± 250 years BP and 39 710 ± 610 years BP) suggests that this highstand occurred before the Last Glacial period. The highest lake level found in our study area is 188 m a.m.l at the eastern rim of the Khyargas Nuur basin (Wolf et al., 2025). However, due to the absence of suitable materials for luminescence dating, no OSL age has been determined for this site. Our results indicate that a large palaeolake, with a level of ~129 m a.m.l, formed during the late last interstadial (~89 ka). During the last interglacial, a large lake covering nearly 600 km^2 with a depth of 17 m was reconstructed at Zavkhan Gol (~114–127 ka, Stolz et al., 2012; Lehmkuhl et al., 2018). A lake highstand (~56 m a.m.l) at Orog Nuur in the Valley of Gobi Lakes, southern Mongolia, has also been dated to MIS 5, though various sub-stages within MIS 5 have been identified (Lehmkuhl et al., 2018; Nottebaum et al., 2022; Zhang et al., 2022b). Lehmkuhl et al. (2018) attributed these high lake levels to a significantly wetter climate, driven by high insolation values during MIS 5.

During the Late Glacial (~14 ka), a palaeolake with a level of 118 m a.m.l developed in Khyargas Nuur. Evidence for a cold and dry Late Glacial period (before 11.5 kyr BP) in Khoton Nuur, western Mongolian Altai, is supported by pollen spectra, indicating the dominance of dry steppe vegetation, and diatom assemblages (Rudaya et al., 2009). Several studies indicate that repeated glacial advances occurred during MIS 3 and MIS 2 in western Mongolia (Rother et al., 2014; Lehmkuhl et al., 2016; Pötsch, 2017; Batbaatar et al., 2018; Blomdin et al., 2018; Strand et al., 2022). The high lake level observed in the Late Glacial period was likely not due to increased precipitation but was instead driven by an increased influx of glacial meltwater from the nearby Altai and Khangai Mountains (Wolf et al., 2025). Notably, no lake highstand records from MIS 3 are preserved along the Khyargas Nuur (Fig. 5), suggesting that lake levels during MIS 3 were lower than the 118 m a.m.l observed in the Late Glacial period, with earlier deposits presumably eroded by subsequent high lake levels. Data from this study also indicate a rapid lake level decline of ~25 m/ka between ~14 and ~11 ka (Fig. 5). The rapid lake level regression during this period is attributed to a combination of factors, notably a transition toward drier post-MIS 2 conditions and a reduction in glacial meltwater inflow (Wolf et al., 2025).

The absence of early and middle Holocene palaeoshoreline records at Khyargas Nuur (Fig. 5) suggests generally low lake levels during these periods. Pollen records from Tolbo and Achit Lakes in the Mongolian Altai indicate predominantly dry conditions with steppe and desert steppe vegetation until ~7–6.5 ka (Sun et al., 2013; Hu et al., 2024). However, wetter conditions during the middle Holocene in western Mongolia cannot be excluded (Zhang and Feng, 2018; Klinge and Sauer, 2019), and more studies are needed. In the late Holocene, small-scale lake level fluctuations were recorded, which can be attributed to short climatic fluctuations during the latest Holocene period (Klinge and Sauer, 2019).

Conclusions

Despite the potential of the Depression of Great Lakes for understanding the late Quaternary hydroclimatic history of western Mongolia, relatively few studies provide robust chronological data for palaeolake reconstruction. This study presents the first detailed luminescence dating investigation of shoreline and lacustrine sediments from Khyargas Nuur in western Mongolia. Whereas the detailed lake level reconstruction and regional climate interpretation are presented in Wolf et al. (2025), the present study provides the detailed methodological basis that underpins those interpretations. By applying both multigrain and single-grain K-feldspar pIRIR dating to 19 sediment samples, we demonstrate the effectiveness of this approach for reliably reconstructing palaeoshoreline chronologies. Results indicate that the pIRIR signal is suitable for dating palaeoshorelines, though problems with incomplete bleaching of pIRIR signals before deposition were identified. Despite this, the application of single-grain analysis and MAM has proven effective in accurately constraining the timing of lake level changes. This methodological refinement is essential, as multigrain D_e distributions can obscure partial bleaching and result in significant age overestimation. We therefore recommend conducting pIRIR dating at the single-grain level for palaeolake shoreline sediments, particularly in depositional environments susceptible to partial bleaching. The resulting chronology provides a reliable temporal framework for lake level changes at Khyargas Nuur, indicating major highstands during MIS 5 and the Late Glacial (~129 m and ~118 m a.m.l, respectively), followed by a rapid regression of ~100 m throughout the Late Glacial to early Holocene transition.

Acknowledgements. This contribution is part of a research project funded by the German Research Foundation (Deutsche

Forschungsgemeinschaft, DFG, ID: 461875474). The authors thank Sabine Mogwitz for the help in luminescence sample preparation and Petra Posimowski for the help in gamma spectrometry measurements. This text was linguistically improved using AI (ChatGPT). Open Access funding enabled and organized by Projekt DEAL.

Data availability statement

The data that support the findings of this study are available from the corresponding author upon reasonable request.

Supporting information

Additional supporting information may be found in the online version of this article at the publisher's website.

Figure S1. Stratigraphic logs of the investigated sites in study areas A (a), B (b), and C (c), modified after Wolf et al. (2025).

Figure S2. (a) Comparison of fading corrected IR_{50} and pIRIR ages for all samples, except for LUM 4719 and 4720, for which different fading correction methods were applied to the IR_{50} and $pIRIR_{225}$ signals. (b) Fading corrected IR_{50} ages, calculated using g_{2days}-values ranging from 1 to 6%/decade, plotted against reference ages (fading corrected pIRIR ages of well-bleached samples).

Figure S3. (a, b) Kernal density estimate (KDE) plots showing the residual dose distributions for samples LUM 4723 (a), and 4724 (b). (c, d) Radial plots displaying the distribution of dose recovery ratios for samples LUM 4723 (c), and 4724 (d).

Figure S4. Abanico plots showing the D_e distribution of K-feldspar single-grains. Bold sample numbers and statistical summaries correspond to well-bleached samples, while those in italics represent poorly-bleached samples. n=number of grains used for D_e calculation (black circles)/number of grains passing standard selection criteria (grey circles). OD values indicate the overdispersion of the grains used for the D_e calculation (black circles). The blue lines represent the arithmetic mean D_e, and the orange lines indicate the MAMD_e.

Figure S5. D_e (in black) and OD (in red) values plotted as a function of T_n threshold for all samples. The dashed lines represent the D_e plateau. Bold sample numbers correspond to well-bleached samples, while those in italics represent poorly-bleached samples.

Table S1. Numbers of K-feldspar grains measured, rejected, and accepted for D_e estimation, along with the reasons for rejection.

Table S2. Summary of IR_{50} results from multi-grain aliquots (2.5 mm).

References

Auclair, M., Lamothe, M. & Huot, S. (2003) Measurement of anomalous fading for feldspar IRSL using SAR. *Radiation Measurements*, 37, 487–492.

Bailey, R.M. & Arnold, L.J. (2006) Statistical modelling of single grain quartz D_e distributions and an assessment of procedures for estimating burial dose. *Quaternary Science Reviews*, 25, 2475–2502.

Batbaatar, J., Gillespie, A.R., Fink, D., Matmon, A. & Fujioka, T. (2018) Asynchronous glaciations in arid continental climate. *Quaternary Science Reviews*, 182, 1–19.

Blomdin, R., Stroeven, A.P., Harbor, J.M., Gribenski, N., Caffee, M.W., Heyman, J. et al. (2018) Timing and dynamics of glaciation in the Ikh Turgen Mountains, Altai region, High Asia. *Quaternary Geochronology*, 47, 54–71.

Buylaert, J.P., Murray, A.S., Thomsen, K.J. & Jain, M. (2009) Testing the potential of an elevated temperature IRSL signal from K-feldspar. *Radiation Measurements*, 44, 560–565.

Chen, F., Chen, J., Huang, W., Chen, S., Huang, X., Jin, L. et al. (2019) Westerlies Asia and monsoonal Asia: Spatiotemporal differences in climate change and possible mechanisms on decadal to sub-orbital timescales. *Earth-Science Reviews*, 192, 337–354. https://doi.org/10.1016/j.earscirev.2019.03.005

Colarossi, D., Duller, G.A.T., Roberts, H.M., Tooth, S. & Lyons, R. (2015) Comparison of paired quartz OSL and feldspar post-IR IRSL dose distributions in poorly bleached fluvial sediments from South Africa. *Quaternary Geochronology*, 30, 233–238.

Deviatkin, E.V., Saitzew, N.S., Kurina, S.S., Florensow, N.A. & Korschnew, S.S. (1987) Geomorphological Map of Socialist Mongolian Republic 1:1.5 Mio. (in Russian).

European Space Agency. (2024) *Copernicus global digital elevation models*. Distributed by Open Topography. Available from: https://doi.org/10.5069/G9028PQB [Accessed 17th December 2024].

Galbraith, R.F., Roberts, R.G., Laslett, G.M., Yoshida, H. & Olley, J.M. (1999) Optical dating of single and multiple grains of quartz from Jinmium rock shelter, northern Australia: part I, experimental design and statistical models. *Archaeometry*, 41, 339–364.

Grunert, J., Lehmkuhl, F. & Walther, M. (2000) Paleoclimatic evolution of the Uvs Nuur basin and adjacent areas (Western Mongolia). *Quaternary International*, 65/66, 171–192.

Guérin, G., Mercier, N., Nathan, R., Adamiec, G. & Lefrais, Y. (2012) On the use of the infinite matrix assumption and associated concepts: a critical review. *Radiation Measurements*, 47, 778–785.

Guo, Y., Li, B. & Zhao, H. (2020) Comparison of single-aliquot and single-grain METpIRIR D_e results for potassium feldspar samples from the Nihewan Basin, northern China. *Quaternary Geochronology*, 56, 101040.

Hu, Y., Huang, X., Demberel, O., Zhang, J., Xiang, L., Gundegmaa, V. et al. (2024) Quantitative reconstruction of precipitation changes in the Mongolian Altai Mountains since 13.7 ka. *Catena*, 234, 107536.

Hülle, D., Hilgers, A., Radtke, U., Stolz, C., Hempelmann, N., Grunert, J. et al. (2010) OSL dating of sediments from the Gobi Desert, Southern Mongolia. *Quaternary Geochronology*, 5, 107–113.

Huntley, D.J. & Baril, M.R. (1997) The K content of the K-feldspars being measured in optical dating or in thermoluminescence dating. *Ancient TL*, 15, 11–13.

Huntley, D.J. & Hancock, R.G.V. (2001) The Rb contents of the K-feldspar grains being measured in optical dating. *Ancient TL*, 19, 43–46.

Huntley, D.J. & Lamothe, M. (2001) Ubiquity of anomalous fading in K-feldspars and the measurement and correction for it in optical dating. *Canadian Journal of Earth Sciences*, 38, 1093–1106.

Jacobs, Z. (2008) Luminescence chronologies for coastal and marine sediments. *Boreas*, 37, 508–535.

Kars, R.H., Wallinga, J. & Cohen, K.M. (2008) A new approach towards anomalous fading correction for feldspar IRSL dating—tests on samples in field saturation. *Radiation Measurements*, 43, 786–790.

Klinge, M. & Lehmkuhl, F. (2013) Geomorphology of the Tsetseg Nuur basin, Mongolian Altai-lake development, fluvial sedimentation and aeolian transport in a semi-arid environment. *Journal of Maps*, 9, 361–366.

Klinge, M. & Sauer, D. (2019) Spatial pattern of Late Glacial and Holocene climatic and environmental development in Western Mongolia—a critical review and synthesis. *Quaternary Science Reviews*, 210, 26–50.

Lehmkuhl, F., Grunert, J., Hülle, D., Batkhishig, O. & Stauch, G. (2018) Paleolakes in the Gobi region of southern Mongolia. *Quaternary Science Reviews*, 179, 1–23.

Lehmkuhl, F., Klinge, M., Rother, H. & Hülle, D. (2016) Distribution and timing of Holocene and late Pleistocene glacier fluctuations in western Mongolia. *Annals of Glaciology*, 57, 169–178.

Lehmkuhl, F., Wolf, D., Boemke, B., Klinge, M., Batkhishig, O. & Grunert, J. (2024) Aeolian sediments in western Mongolia: distribution and (paleo)climatic implications. *Geomorphology*, 465, 109407.

Li, B., Jacobs, Z., Roberts, R.G. & Li, S.-H. (2018) Single-grain dating of potassium-rich feldspar grains: towards a global standardised growth curve for the post-IR IRSL signal. *Quaternary Geochronology*, 45, 23–36.

Li, B., Roberts, R.G., Jacobs, Z., Li, S.H. & Guo, Y.J. (2015) Construction of a 'global standardised growth curve' (gSGC) for infrared stimulated luminescence dating of K-feldspar. *Quaternary Geochronology*, 27, 119–130.

Li, Y., Tsukamoto, S., Klinge, M., Sauer, D. & Frechen, M. (2023) K-feldspar $pIRIR_{150}$ dating of the Late Pleistocene sediments in the

NW Khangai Mountains (Mongolia) using a standardized dose-response curve approach. *Frontiers in Earth Science*, 10, 939852.

Liritzis, I., Stamoulis, K., Papachristodoulou, C. & Ioannides, K. (2013) A re-evaluation of radiation dose-rate conversion factors. *Mediterranean Archaeology Archaeometry* 13, 1–15.

Long, H., Haberzettl, T., Tsukamoto, S., Shen, J., Kasper, T., Daut, G. et al. (2015) Luminescence dating of lacustrine sediments from Tangra Yumco (southern Tibetan Plateau) using post-IR IRSL signals from polymineral grains. *Boreas*, 44, 139–152.

Murray, A.S. & Wintle, A.G. (2000) Luminescence dating of quartz using an improved single-aliquot regenerative-dose protocol. *Radiation Measurements*, 32, 57–73.

Murray, A.S., Thomsen, K.J., Masuda, N., Buylaert, J.-P. & Jain, M. (2012) Identifying well bleached quartz using the different bleaching rates of quartz and feldspar luminescence signals. *Radiation Measurements*, 47, 688–695.

Naumann, S. (1999) Spät- und postglaziale Landschaftsentwicklung im Bajan Nuur Seebecken (Nordwestmongolei) Late- and postglacial landscape evolution in the Bay an Nuur lake basin (northwestern Mongolia). *Die Erde*, 130, 117–130.

Nottebaum, V., Stauch, G., van der Wal, J.L.N., Zander, A., Schlütz, F., Shumilovskikh, L. et al. (2022) Late Quaternary landscape evolution and paleoenvironmental implications from multiple geomorphic dryland systems, Orog Nuur Basin, Mongolia. *Earth Surface Processes and Landforms*, 47, 275–297.

Orkhonselenge, A., Uuganzaya, M. & Davaagatan, T. (2022) Landscape, lake distribution, and evolution in western Mongolia. In: *Lakes of Mongolia*. Syntheses in Limnogeology. Berlin, Heidelberg: Springer, pp. 179–201.

Peng, J. & Li, B. (2017) Single-aliquot regenerative-dose (SAR) and standardised growth curve (SGC) equivalent dose determination in a batch model using the R Package 'numOSL'. *Ancient TL*, 35, 32–53.

Pötsch, S. (2017) Dynamics and paleo-climatic forcing of Late Pleistocene Glaciers in the Turgen and Khangai Mountains (Mongolia) reconstructed from geomorphology, ^{10}Be surface exposure dating, and ice flow modeling. PhD Thesis, University of Greifswald.

Prescott, J.R. & Hutton, J.T. (1994) Cosmic ray contributions to dose rates for luminescence and ESR dating large depths and long-term time variations. *Radiation Measurements*, 23, 497–500.

Reimann, T. & Tsukamoto, S. (2012) Dating the recent past (<500 years) by post-IR IRSL feldspar–examples from the North Sea and Baltic Sea coast. *Quaternary Geochronology* 10, 180–187.

Reimann, T., Thomsen, K.J., Jain, M., Murray, A.S. & Frechen, M. (2012) Single-grain dating of young sediments using the pIRIR signal from feldspar. *Quaternary Geochronology*, 11, 28–41.

Rhodes, E.J. (2011) Optically stimulated luminescence dating of sediments over the past 200,000 years. *Annual Review of Earth and Planetary Sciences*, 39, 461–488.

Rother, H., Lehmkuhl, F., Fink, D. & Nottebaum, V. (2014) Surface exposure dating reveals MIS-3 glacial maximum in the Khangai Mountains of Mongolia. *Quaternary Research*, 82, 297–308.

Rudaya, N., Tarasov, P., Dorofeyuk, N., Solovieva, N., Kalugin, I., Andreev, A. et al. (2009) Holocene environments and climate in the Mongolian Altai reconstructed from the Hoton-Nur pollen and diatom records: a step towards better understanding climate dynamics in Central Asia. *Quaternary Science Reviews*, 28, 540–554.

Stolz, C., Hülle, D., Hilgers, A., Grunert, J., Lehmkuhl, F. & Dasch, D. (2012) Reconstructing fluvial, lacustrine and aeolian process dynamics in Western Mongolia. *Zeitschrift für Geomorphologie*, 56, 267–300.

Strand, P.D., Putnam, A.E., Sambuu, O., Putnam, D.E., Denton, G.H., Schaefer, J.M. et al. (2022) A ^{10}Be Moraine Chronology of the last Glaciation and termination at 49° N in the Mongolian Altai of Central Asia. *Paleoceanography and Paleoclimatology*, 37, e2022PA004423.

Sun, A., Feng, Z., Ran, M. & Zhang, C. (2013) Pollen-recorded bioclimatic variations of the last ~22,600 years retrieved from Achit Nuur core in the western Mongolian Plateau. *Quaternary International*, 311, 36–43.

Thomsen, K.J., Murray, A.S., Jain, M. & Bøtter-Jensen, L. (2008) Laboratory fading rates of various luminescence signals from feldspar-rich sediment extracts. *Radiation Measurements*, 43, 1474–1486.

Wolf, D., Lehmkuhl, F., Schaubert, V., Rahimzadeh, N., Frechen, M., Stauch, G. et al. (2025) Drivers of late Quaternary lake level fluctuations of Khyargas Nuur, western Mongolia—glacial meltwater discharge or atmospheric moisture supply? *Quaternary Science Reviews*, 359, 109373.

Zhang, D. & Feng, Z. (2018) Holocene climate variations in the Altai Mountains and the surrounding areas: a synthesis of pollen records. *Earth-Science Reviews*, 185, 847–869.

Zhang, S., Zhao, H., Sheng, Y., Chen, S., Li, G. & Chen, F. (2022b) Late Quaternary lake level record of Orog Nuur, southern Mongolia, revealed by optical dating of paleoshorelines. *Quaternary Geochronology*, 72, 101370.

Zhang, S., Zhao, H., Sheng, Y., Zhang, J., Zhang, J., Sun, A. et al. (2022a) Mega-lakes in the northwestern Tibetan Plateau formed by melting glaciers during the last deglacial. *Quatenary Science Reviews*, 285, 107528.